Actin turnover ensures uniform tension distribution during cytokinetic actomyosin ring contraction

Thomas H. Cheffings[a,b], Nigel J. Burroughs[b,c], and Mohan K. Balasubramanian[a,*]
[a]Centre for Mechanochemical Cell Biology and Division of Biomedical Sciences, Warwick Medical School,
[b]Zeeman Institute, and [c]Mathematics Institute, University of Warwick, Coventry CV4 7AL, United Kingdom

ABSTRACT In many eukaryotes, cytokinesis is facilitated by the contraction of an actomyosin ring (AMR). The exact mechanisms that lead to this contractility are unknown, although some models posit that actin turnover in the AMR is essential. The effect of reduced actin dynamics during AMR formation has been well studied in *Schizosaccharomyces pombe*; however, the corresponding effects on AMR contraction are not well understood. By using mutants of the fission yeast actin severing protein Adf1, we observed that contracting AMRs display a "peeling" phenotype, where bundles of actin and myosin peel off from one side of the AMR, and are pulled across to the opposite side. This occurs multiple times during cytokinesis and is dependent on the activity of myosins Myo2, Myp2, and Myo51. We found that the distribution of Myo2 in the AMR anticorrelates with the location of peeling events, suggesting that peeling is caused by a nonuniform tension distribution around the AMR, and that one of the roles of actin turnover is to maintain a uniform tension distribution around the AMR.

INTRODUCTION

A contractile actomyosin ring (AMR) is essential for normal cytokinesis in fungal, amoeboid, and metazoan cells, and both extensive investigation of model organisms and theoretical modeling have provided a partial picture of its formation and contraction (Pollard, 2010; Green *et al.*, 2012; Cheffings *et al.*, 2016). The fission yeast *Schizosaccharomyces pombe* is a valuable system for the characterization of mechanisms regulating AMR function, but while much is known about AMR positioning and assembly, the mechanisms that enable ring contraction are only now beginning to emerge (Cheffings *et al.*, 2016; Pollard, 2017).

It is known that many components of the AMR undergo rapid turnover (Yumura, 2001; Pelham and Chang, 2002; Murthy and Wadsworth, 2005; Srivastava and Robinson, 2015), and a number of computational models posit that this dynamism is necessary for tension generation within AMRs (Stachowiak *et al.*, 2014; Oelz *et al.*, 2015; Thiyagarajan *et al.*, 2017; Nguyen *et al.*, 2018). However, experiments where turnover is perturbed during AMR contraction have been scarce. Recent work in *Schizosaccharomyces japonicus* found that reducing actin turnover during AMR contraction could rescue the effect of latrunculin A treatment (Chew *et al.*, 2017), which blocks F-actin polymerization and results in AMR disintegration. From this it was proposed that one role of turnover is to maintain actin filament homeostasis in the AMR, thus when the entry of new actin into the AMR is blocked this homeostasis can be synthetically maintained by also blocking disassembly and removal of actin from the AMR (Chew *et al.*, 2017).

In *S. pombe*, actin turnover is primarily regulated by the cofilin Adf1. Previous work has focused on its role in AMR formation, where actin severing is thought to work as an error-correction mechanism during the coalescence of cortical nodes into a uniform AMR (Vavylonis *et al.*, 2008; Chen and Pollard, 2011). We used *adf1* mutants to investigate the effect of reduced actin turnover on AMR contraction and found that this causes a ring peeling phenotype, which seems to be due to a nonuniform distribution of tension around the AMR.

Abbreviations used: AMR, actomyosin ring; CDF, cumulative distribution function; CW, calcofluor white; GMM, Gaussian mixture model; LAGFP, LifeAct-GFP; Lat A, latrunculin A; mNG, mNeonGreen; PDF, probability density function; tdT, tdTomato; TS, temperature sensitive; WT, wild type.

RESULTS AND DISCUSSION

We utilized two mutants of *S. pombe* Adf1, Adf1-M2 and Adf1-M3, which were shown to have reduced F-actin binding affinities and severing rates (Chen and Pollard, 2011), causing reduced actin turnover in cells (Supplemental Figure S1A). Visualizing AMR contraction face-on in *adf1*-M2 and *adf1*-M3 cells, we observed that bundles of myosin and (presumably) actin peeled off from one side of the AMR, and were pulled in toward the opposite side (Figure 1A), behavior that was not seen in wild-type (WT) cells (Figure 1B). We also noticed that some of these peeling bundles snapped when they were partway across the AMR (Figure 1C): the breakage occurred at one of the attachment points, and then the bundle was "reeled in" to the AMR through its remaining attachment point. We refer to this as "snapping-and-reeling," while we refer to peeling bundles that do not snap as "unbroken peeling."

We analyzed the percentage of AMRs displaying a peeling phenotype in *adf1*-M2, *adf1*-M3, and WT cells, while also quantifying the relative proportion of each subphenotype (Figure 1F). In WT cells, we observed a small proportion of AMRs displaying some snapping-and-reeling; however, these bundles were not as noticeable as they were in the *adf1* mutants (Figure 1G), and the majority of AMRs did not show any peeling behavior. By contrast, in *adf1*-M2 and *adf1*-M3 cells, nearly 100% of AMRs displayed some form of peeling, the most common being unbroken peeling, with some snapping-and-reeling events being observed, and a small amount of AMRs displaying a continuous peeling phenotype, consisting of multiple rapid peeling events (Figure 1F).

From AMR contraction kymographs, we noticed that in most AMRs there were three or four peeling events during cytokinesis (Figure 1A). Counting the number of peeling events, we found that *adf1*-M2 and *adf1*-M3 cells undergo an average of three events (Figure 1H). By measuring the angular separation between consecutive peeling events, we also found that 80–90% of peeling events in *adf1*-M2 and *adf1*-M3 cells started from the opposite side of the AMR relative to the previous event (Figure 1I). Correspondingly, we found that peeling initiation occurred in the neighborhood of the previous event's merger point with the AMR (Supplemental Figure S1B).

Because Adf1 function is also important for AMR formation (Nakano and Mabuchi, 2006; Chen and Pollard, 2011), it was possible that ring peeling could be caused by defective AMR formation, rather than reduced actin turnover during AMR contraction. To rule this out, we used a strain containing the temperature-sensitive (TS) *adf1*-1 mutation in conjunction with the cold-sensitive tubulin mutation *nda3*-KM311. By blocking cells in metaphase at 18°C, and then shifting to the *adf1*-1 restrictive temperature, we generated AMRs that were formed with relatively normal Adf1 function, but contracted under impaired Adf1 function.

Shifting metaphase-arrested WT cells to 36°C caused AMRs to fall apart; however, when shifted to 30°C the AMRs remained intact, and in *adf1*-1 cells we observed ring peeling (Figure 1D), which was reduced in control cells (Figure 1E). Almost 100% of AMRs in *adf1*-1 cells exhibited a peeling phenotype, with the majority displaying continuous peeling (Figure 1F). This made it difficult to identify individual peeling events, which precluded quantifying the number of peeling events and their angular separation in these cells. In control cells we detected a relatively high proportion of AMRs undergoing peeling (Figure 1F; 48%); however, similar to what we observed in WT cells, these bundles only peeled off a short distance before snapping (similar to Figure 1G), so they were not as readily visible as the events in *adf1*-1 cells.

Because of the difference in peeling phenotypes that distinguish *adf1*-M2 and *adf1*-M3 from *adf1*-1 cells, we cannot conclude that the peeling phenotype in *adf1*-M2 and *adf1*-M3 cells is solely because of reduced actin turnover during AMR contraction. However, on the basis of the results from *adf1*-1 cells, we can say that peeling does occur in AMRs where actin turnover is only reduced during contraction.

We next wondered whether peeling events in *adf1*-M2 and *adf1*-M3 cells occur randomly, or whether they occur at specific times relative to the onset of AMR contraction. To investigate this, we collected four-dimensional images of *adf1*-M2 and *adf1*-M3 cells, and selected cells where AMR contraction did not begin until >20 min after the start of the acquisition, to ensure we observed the first peeling event. Then, we measured the timing of the first three peeling events in these cells. If these times were random, we would expect the data to exhibit a flat distribution, but instead we observed that histograms for both strains showed three main peaks (Figure 2A), indicating that peeling events occur at predictable times. To further support this, we fitted a Gaussian mixture model (GMM) to each data set, comparing models with between one and five components, and using the Akaike Information Criterion to determine the optimum model. For both strains, we found that a three-component model was the *best* fit, while the fitted three-component model probability density functions (PDFs) also reproduced the histogram patterns, suggesting that they are a *good* fit (Figure 2A). Because the appearance of a histogram depends on the binning used, we also plotted the model cumulative distribution functions (CDFs) alongside the empirical CDFs of the data, as the appearance of the empirical CDF is completely determined by the data. These plots showed excellent agreement between the model and the data (Figure 2B), and making P-P plots further reinforced this (Figure 2B, insets). Overall, this analysis indicates that peeling events are not random but instead occur at predictable times relative to the onset of AMR contraction.

As Rlc1 is a light chain for both myosin II heavy chains, Myo2 and Myp2, we decided to separately tag these proteins, in order to see which of them localize to peeling bundles. Using GFP-Myo2, we observed no peeling in *adf1*-M3 and *adf1*-1 cells (Figure 3A and Supplemental Figure S1C); however, when using Myp2-mNG (mNeonGreen) we observed peeling in both strains, with the majority of Myp2 being pulled off of the AMR with the peeling bundle (Figure 3B and Supplemental Figure S1D). Tagging both proteins with different fluorophores further confirmed that Myp2, but not Myo2, was present on peeling bundles (Figure 3C).

This suggested that Myp2 may be needed for peeling. We investigated the effect of *myp2* deletion on ring peeling, using LifeAct-GFP (LAGFP) as an AMR marker, as this binds directly to actin. We observed no peeling in WT cells (Figure 3D), while peeling was visible in *adf1*-M3 cells (Figure 3E). In *adf1*-M3 *myp2Δ* cells we saw a distinct reduction in the amount of peeling, with only occasional and very faint events observed (Figure 3F).

We also decided to see whether deleting *myo51* had an effect on peeling in *adf1*-M3 cells: As Myo51 is thought to mainly function during AMR formation, we expected its absence to have very little effect (Laplante *et al.*, 2015). However, in *adf1*-M3 *myo51Δ* cells, we found that the peeling bundles also appeared to be fainter, although their frequency was increased (Figure 3G), somewhat resembling the continuous peeling in *adf1*-1 cells (Figure 1D). Checking the localization of Myo51 in *adf1*-M3 cells, we found that it localizes to peeling bundles; however, a large amount also remains on the AMR (Supplemental Figure S1E), unlike Myp2.

Subsequently, we checked whether Myo2, the only other myosin in the AMR, also plays a role in ring peeling. Using the TS mutant
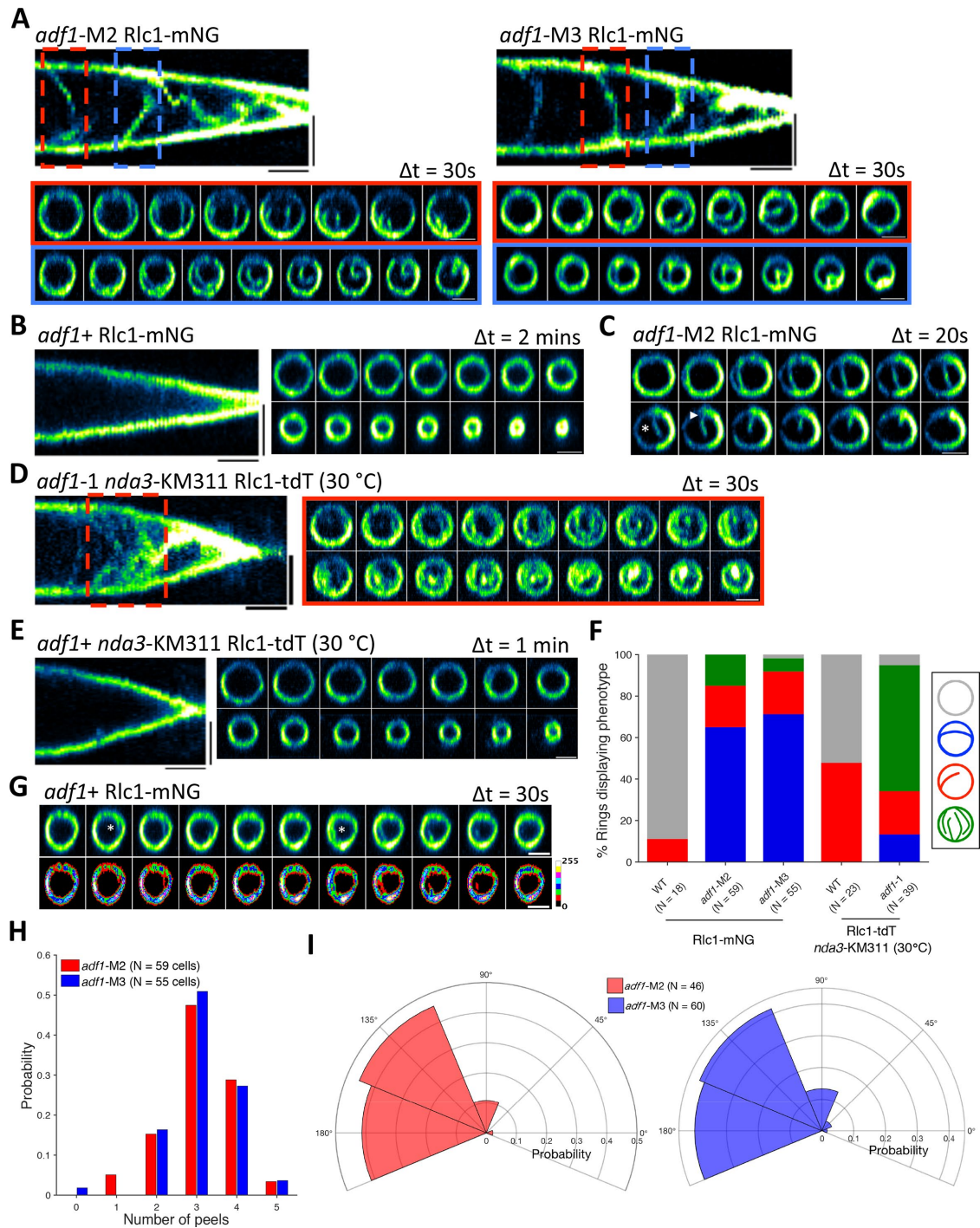
FIGURE 1: *adf1* mutant cells display a peeling phenotype during ring contraction. (A) Kymographs and montages of contracting AMRs in *adf1*-M2 and *adf1*-M3 cells. (B) Kymograph and montage of a contracting AMR in a WT cell (control for A). (C) Montage of a peeling event where the bundle snaps at one end (asterisk) and is then reeled in at its remaining attachment point (arrowhead). (D) Kymograph and montage of a contracting AMR in an *adf1*-1 cell. (E) Kymograph and montage of a contracting AMR in an *adf1*+ cell (control for D). (F) Quantification of relative proportions of subphenotypes observed in each strain, denoted by the color coding of the bars (no phenotype, gray; unbroken peeling, blue; snapping-and-reeling, red; continuous peeling, green). (G) Montage of minor peeling events (asterisks) that occur in a subset of WT cells. Second row corresponds to the first, but using a false-color LUT. (H) Histogram of the number of peeling events (only unbroken peeling and snapping-and-reeling) observed in *adf1*-M2 and *adf1*-M3 cells. (I) Polar histograms of the angular distribution of peeling events (only unbroken peeling, and snapping-and-reeling), measured relative to the preceding event (i.e., 0°). Scale bars are 2 μm in montages and 2 μm and 5 min in kymographs.
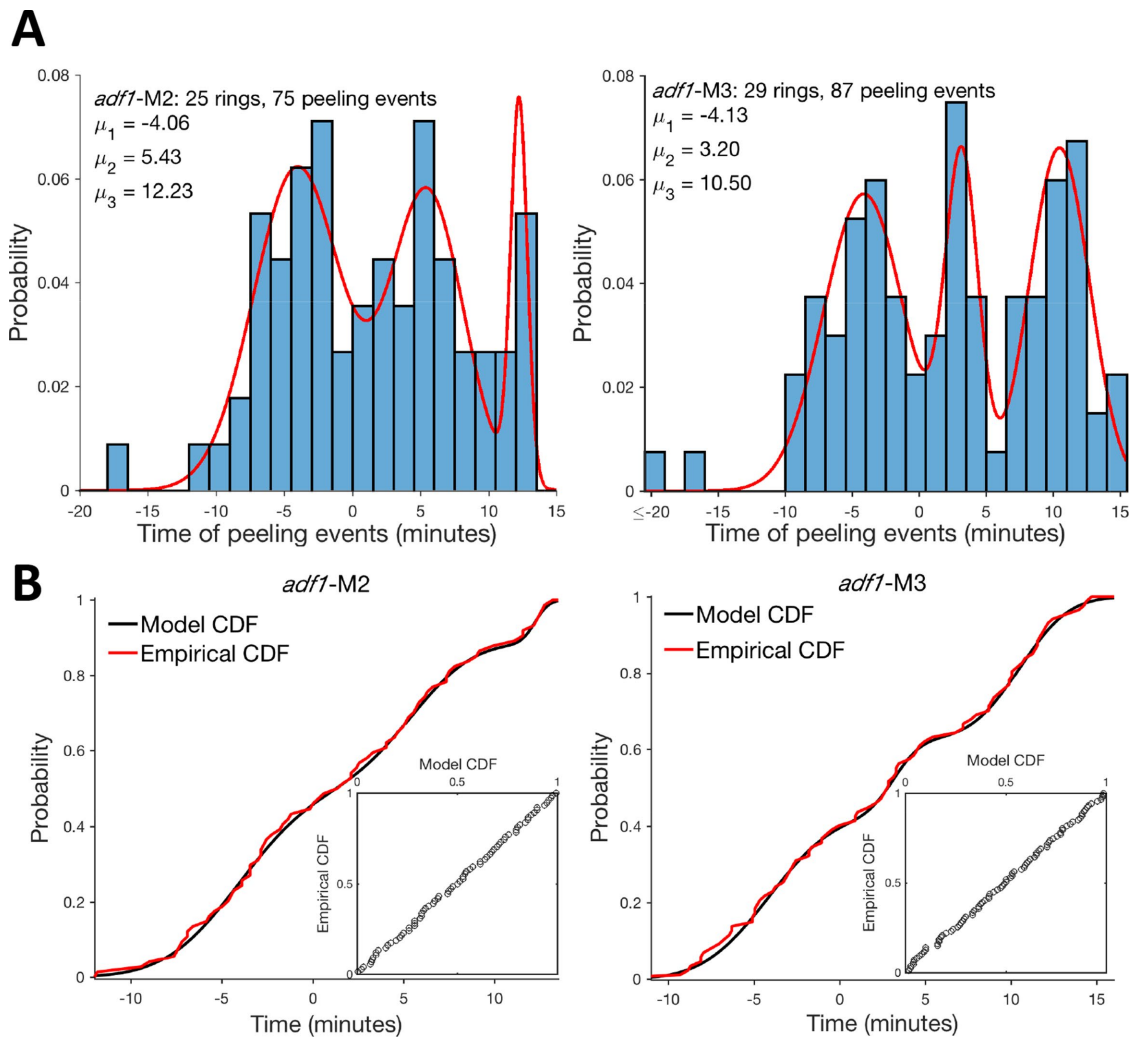
FIGURE 2: Peeling events occur at nonrandom times. (A) Histograms of the times at which the first three peeling events occur in *adf1*-M2 and *adf1*-M3 cells, relative to the onset of AMR contraction. The PDF of the optimal three-component GMM is overlaid, and the centers of the three components are listed on the graph (analysis excluded outlier events occurring at times < −15 min). (B) Plots of the CDF from our three-component GMMs overlaid with the empirical CDF of the data. Insets are P-P plots.

myo2-E1 at the semirestrictive temperature of 30°C, we observed an almost complete absence of peeling, with the few observed peeling events also being very faint (Figure 3H). In combination, these experiments show that ring peeling is dependent, to various degrees, on the activity of all three myosins, although only Myp2 and Myo51 were clearly detected in the peeling bundles.

Because previous work has shown that actin turnover is necessary for the stable generation of tension in AMRs (Stachowiak *et al.*, 2014; Oelz *et al.*, 2015; Thiyagarajan *et al.*, 2017; Nguyen *et al.*, 2018), we hypothesized that reduced actin turnover might lead to a more heterogeneous distribution of tension around the AMR. Then, because regions of higher tension would experience a greater inward force (Thiyagarajan *et al.*, 2015) compared with other parts of the AMR, we predicted that this could cause actin filaments in these regions to undergo peeling.

To test this model, we first looked at the distribution of myosin and actin around the AMR, as a nonuniform distribution of these proteins would be indicative of a nonuniform tension distribution. We have already seen that Myp2 localizes inhomogeneously, favorably localizing to the peeling bundles (Figure 3B).

To investigate the distribution of Myo2, we constructed normalized intensity kymographs of contracting AMRs (see *Materials and Methods*) using GFP-Myo2 in WT and *adf1*-M3 cells. In WT cells we observed a relatively uniform distribution of Myo2; however, in *adf1*-M3 cells the Myo2 was distributed inhomogeneously, in patterns that often seemed to move around the AMR (Figure 4A). Because of anisotropy in the microscope point spread function (PSF), the signal is slightly poorer at the top and bottom of the AMR (90°, 270°).

We next examined the distribution of actin, using LAGFP. We used a similar method as before; however, we first segmented the AMRs (see *Materials and Methods*) using the fluorescence from Cdc15-tdT, so that we could remove the signal from actin patches and cables near the AMR (Courtemanche *et al.*, 2016). In WT cells we again observed a uniform protein distribution around the AMR (Supplemental Figure S1F). In *adf1*-M3 cells, the distribution of LAGFP AMR fluorescence appeared less uniform than in WT cells (Supplemental Figure S1F). However, the degree of heterogeneity was less than was observed when using GFP-Myo2 (compare Figure 4A and Supplemental Figure S1F).
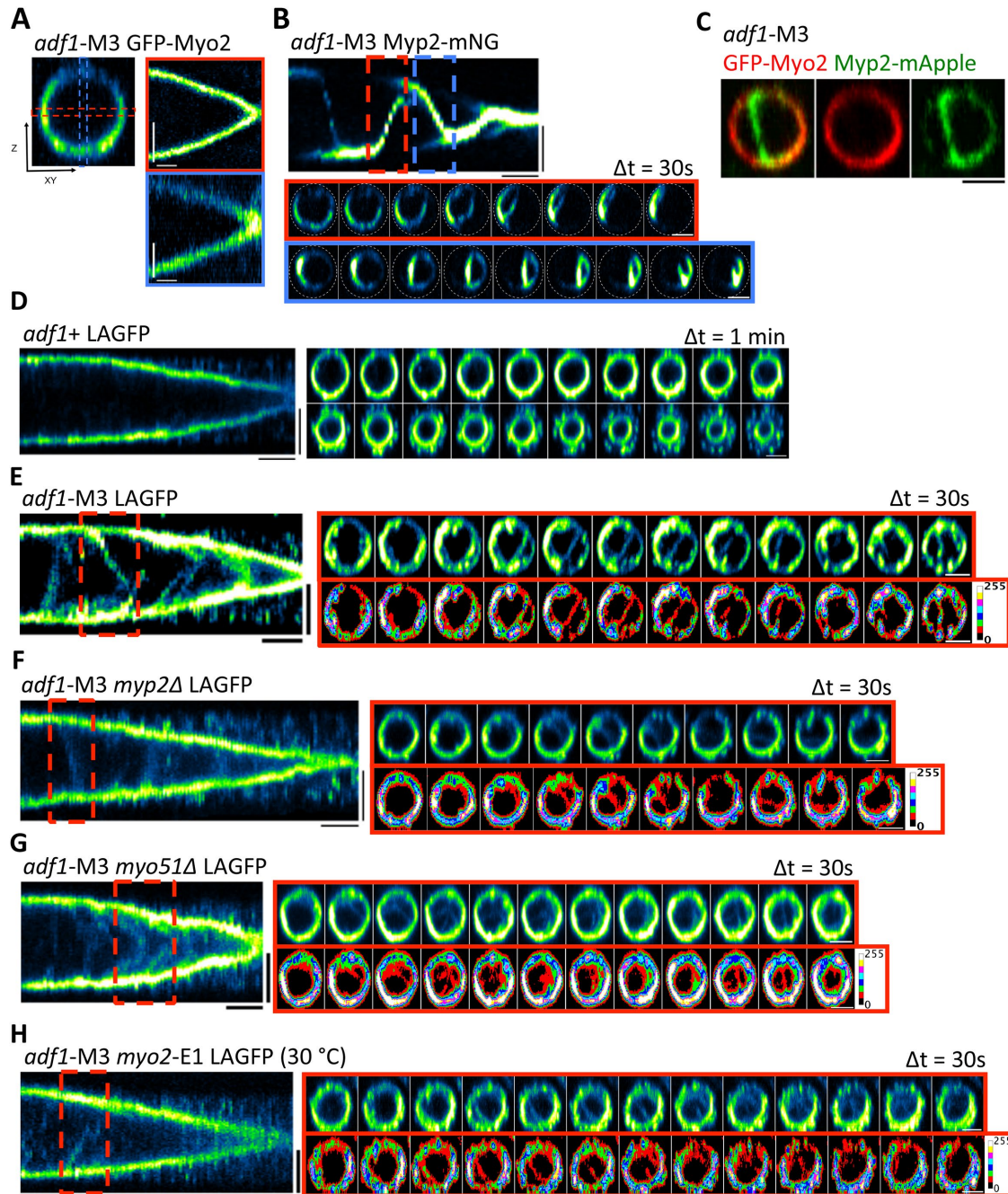
FIGURE 3: Ring peeling depends on the presence of Myo2, Myp2, and Myo51. (A) Kymographs in two perpendicular directions of a contracting AMR in an *adf1*-M3 GFP-Myo2 cell. (B) Kymograph and montages of AMR contraction in an *adf1*-M3 Myp2-mNG cell. (C) Single timepoint image of a peeling AMR in an *adf1*-M3 GFP-Myo2 Myp2-mApple cell. (D–H) AMR contraction kymographs and montages of cells expressing LAGFP, with the following genotypes: (D) WT, (E) *adf1*-M3, (F) *adf1*-M3 *myp2Δ*, (G) *adf1*-M3 *myo51Δ*, and (H) *adf1*-M3 *myo2*-E1. In F, G, and H, the second montage is the same as the first, but using a false-color LUT to make faint peeling events more visible. Scale bars are 2 μm in montages and 2 μm and 5 min in kymographs.

Having shown that the *adf1*-M3 mutation leads to increased heterogeneity in the distribution of myosin and (to a lesser extent) actin around the AMR, we then investigated the relation between the distribution of Myo2 and the locations of peeling events. Using strains expressing fluorescently tagged Myo2 and Myp2, we found that regions of high Myo2 intensity anticorrelate with the locations of peeling events (Figure 4B). The lower levels of heterogeneity of

LAGFP around the AMR prevented a similar analysis between actin redistribution and peeling events.

Because our data suggest that tension is an important determinant of peeling, we sourced evidence of nonuniform tension distribution around AMRs in *adf1* mutant cells. Because septation is thought to be locally regulated by AMR tension (Thiyagarajan et al., 2015), we decided to fix WT, *adf1*-M2, and *adf1*-M3 cells,

Actin turnover in cytokinetic fidelity | **937**
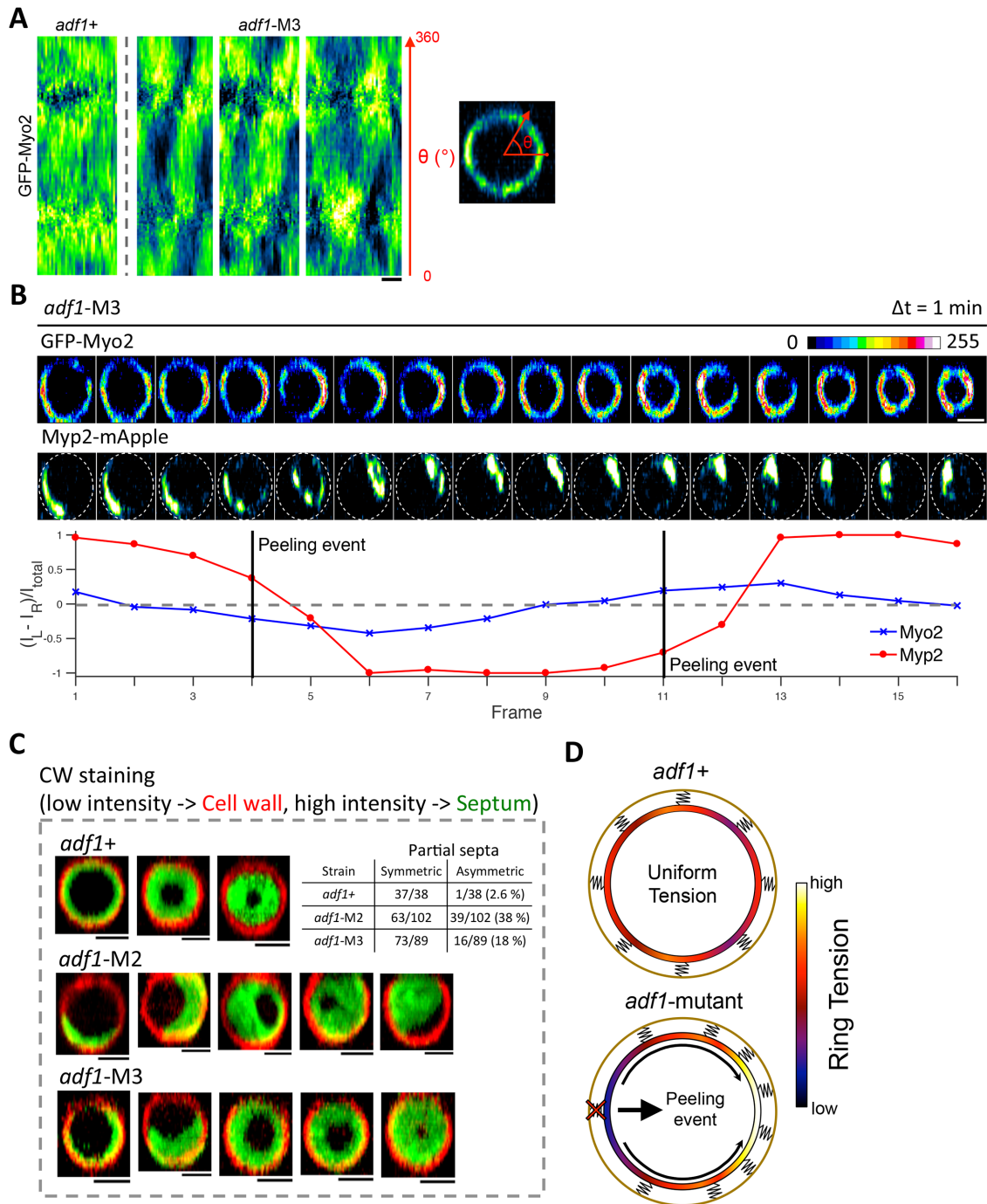
FIGURE 4: Ring peeling in *adf1* mutant cells can be explained by a nonuniform distribution of ring tension. (A) Normalized intensity kymographs of GFP-Myo2 fluorescence in contracting AMRs in WT and *adf1*-M3 cells. Scale bar is 5 min. (B) Montage of peeling events in an *adf1*-M3 cell with GFP-Myo2 and Myp2-mApple. Scale bar is 2 μm and applies to both montages. Graph plots the intensity difference between the left and right sides of the AMR shown in the montage. (C) Representative images of partially septated, CW stained cells. Images have been segmented into low- and high-intensity regions, to represent the outer cell wall and the division septum, respectively. Table shows the proportion of asymmetric septa in each strain. Scale bars are 2 μm. (D) Diagram of proposed ring peeling mechanism in cells with reduced Adf1 activity: A cross-sectional view of a dividing cell is shown, with the AMR color-coded according to its local tension and springs representing attachments between the AMR and the membrane.

and stain with calcofluor white (CW) to look for partially septated cells where the septa had grown asymmetrically (Figure 4C). In WT cells we observed only 1/38 (2.6%) partially septated cells with asymmetric septum deposition. By contrast, in *adf1*-M3

cells we found that 16/89 (18%) partially septated cells displayed asymmetric septum deposition, while in *adf1*-M2 cells this increased to 39/102 (38%) partially septated cells. These observations support the idea that a nonuniform distribution of myosin

in the AMR also leads to a nonuniform tension distribution around the AMR.

Myo2 is reported to be the main contributor to AMR tension (Zambon *et al.*, 2017). Thus, contrary to the original hypothesis leading up to the experiments in Figure 4, our observations suggest that two factors contribute to peeling: First, the region of highest tension exerts a pulling force on its neighboring regions, which is transmitted around the AMR, so that the region directly opposite is subsequently pulled apart in both directions. The sum of these two forces would lead to a net force that is directed across the AMR, toward the region of highest tension (Figure 4D). Second, because Myo2 is also likely to play a role in linking the AMR to the membrane (Laplante *et al.*, 2016; McDonald *et al.*, 2017), there will also be fewer AMR-membrane connections in the region of lowest Myo2 intensity, which increases the ease with which actomyosin bundles can be peeled off from this region (Figure 4D). Therefore, we propose that the combination of these two effects leads to peeling events occurring at the region of lowest tension in the AMR, and being pulled across to the region of highest tension (Figure 4D).

Our model of ring peeling was inspired by recent work in *Drosophila* embryos, examining the role of actin dynamics during gastrulation (Jodoin *et al.*, 2015). In this study, actin turnover was perturbed by using RNAi to target proteins involved in actin turnover, and injecting embryos with drugs that perturb actin dynamics. By doing so, it was found that when actin turnover was reduced the balance of tension along the apical surface was lost, and epithelial cells would often become stretched and distorted as a result (Jodoin *et al.*, 2015). Although this work demonstrates the effect of tension heterogeneity at a larger scale, a similar model could also explain our observations in *S. pombe* AMRs. Whether a nonuniform tension distribution is a common result of reduced turnover in contractile actomyosin systems remains unclear, and can possibly be investigated using mathematical modeling approaches.

We observed that myosin and actin localize in a nonuniform manner around the AMR in *adf1*-M3 cells, and that the distribution of Myo2 anticorrelates with the location of peeling events. Movement of actin and myosin clusters around the *S. pombe* AMR has been observed previously in WT cells (Wollrab *et al.*, 2016); however, this motion was much faster than what we observed in *adf1*-M3 cells (Figure 4A). Additionally, we only saw a single region of high intensity, whereas multiple foci of high intensity were seen in WT cells (Wollrab *et al.*, 2016). Perhaps the behavior we observed in *adf1* mutant cells is a more extreme version of the behavior in WT cells, with increased clustering and reduced speed of myosin clusters leading to a single region of high tension. It is currently unclear whether the apparent periodicity of Myo2 cluster movement in Figure 4 is through a feedback process with the consecutive peeling events or whether peeling tracks Myo2 redistribution driven independently of peeling.

Based on our data, Myo2 is the most likely candidate for directly causing the observed peeling-off and reeling-in of actomyosin bundles (Figure 4, B and D). This raises the question of what roles Myp2 and Myo51 play in peeling. It is possible that they work together to cross-link the bundles; however, this does not explain the effect of Myo51 deletion on peeling (Figure 3F), as there are thought to be five times fewer molecules of Myo51 in the AMR than there are of Myp2 (Wu and Pollard, 2005; Wang *et al.*, 2014), suggesting that the reduction in cross-linking should be minimal.

Nonetheless, the requirement that all three myosins are present explains why peeling does not start until the final myosin, Myp2,

arrives in the AMR (Figure 2A; Wu *et al.*, 2003). This sets the time of the first peeling event, while the timing of subsequent events is set by the time that it takes for the bundle from the previous event to move across the AMR, and for myosin to subsequently redistribute itself around the AMR (Figures 3B and 4B). This is in agreement with our observations that peeling events occur at predictable times (Figure 2A).

MATERIALS AND METHODS

Yeast strains, medium, and culture conditions
S. pombe strains used are listed in Supplemental Table 1. Cells were cultured in rich medium YEA (5 g/l yeast extract, 30 g/l glucose, and 225 mg/l adenine) until mid–log phase at 24°C for analysis under the microscope. Standard fission yeast genetic and molecular biology protocols were used as previously described (Moreno *et al.*, 1991).

Imaging sample preparation
For imaging non-TS/cold-sensitive cells, 1 ml of mid–log phase cells were concentrated by centrifugation at 2200 rpm for 2 min at room temperature, and then concentrated cells (1–1.5 µl) were placed on a concave glass slide with YEA + 2% agarose pad, and then sealed under a coverslip using VALAP (Vaseline, lanolin, and paraffin). For imaging TS/cold-sensitive cells, the culture was first incubated at the appropriate temperature for a length of time, ~3 h for Myo2-E1 mutants, and until >50% of cells contained a ring for Nda3-KM311 mutants (normally achieved after 6 h incubation). Cells were then concentrated as before, with the centrifuge set to the appropriate temperature, and ~10–20 µl of cells was loaded onto an Ibidi µ-slide eight-well glass bottom dish, which was then sealed off with an adhesive film membrane.

Latrunculin A treatment, cell fixation, and CW staining
For latrunculin A treatment and fixation, 5–10 ml of mid–log phase culture was spun down and resuspended in 1 ml YEA. To this, latrunculin A was added to produce the desired final concentration, and the cells were incubated on a shaker at 24°C for the desired amount of time. For fixation, the cells were then spun down, and resuspended in 0.5 ml 1× phosphate-buffered saline (PBS) + 0.5 ml of 8% paraformaldehyde, and fixed on a shaker at 24°C for 12 min, before washing with PBS. For staining with CW, fixed cells (prepared from 10 ml mid–log phase culture) were resuspended in 25 µl of PBS, and then 2 µl CW at 500× dilution was added to 10 µl of cells. For imaging fixed cells, these were placed on bare microscope slides, and then sealed under a coverslip using VALAP.

Spinning-desk confocal microscopy
All imaging in this article was performed using an Andor Revolution XD spinning-disk confocal microscope system. This was equipped with a Nikon ECLIPSE Ti inverted microscope, Nikon Plan Apo Lambda 100×/1.45 NA oil immersion objective lens, a spinning-disk system (CSU-X1; Yokogawa), and an Andor iXon Ultra EMCCD camera. Images in Figures 1, A–C and G, 3, C–F, and 4B and Supplemental Figure S1, C and F, were obtained at a pixel size of 80 nm. Images in Figures 1, D and E, 3, A, B, G, and H, and 4A and Supplemental Figure S1, A, D, and E, were obtained at a pixel size of 69 nm. Images were acquired with a z-spacing of 0.3 µm, and time-lapse images were obtained at a range of time intervals, usually 30 s, except for Figure 1D, which was acquired with 20 s intervals, and the data used in Figure 2 (unpublished data), which were acquired at 90 s intervals. Two laser lines at wavelengths of 488 and 561 nm were used for excitation.

Image processing

All image processing was performed in FIJI. All images were background subtracted (FIJI/Process/Subtract background). Face-on views of contracting AMRs were generated using the "Reslice" function (Image/Stacks/Reslice…), with a spacing of 0.1 or 0.15 μm, and the resulting images were then maximum intensity projected. Kymographs in Figure 3A and Supplemental Figure S1C were generated from face-on images, using two sets of perpendicular rectangular regions of interest (ROIs). All other kymographs were generated from z-stack images, using a rectangular ROI in the central plane of the ring. The LUT used in the false-color images in Figure 3, F, G, and H, was "brgbcmyw," and the LUT in Figure 4B was "16 colors." The intensity calibration bars in these images were inserted using the "Calibration Bar…" function (Analyze/Tools/Calibration Bar…).

Ring quantification

For measurement of ring contraction rates, the diameter over the course of ring contraction was measured manually from four-dimensional images of contracting AMRs in FIJI. These data were converted to circumference, and then a straight line was fitted to the data in Excel, and the gradient of this line was taken as the contraction rate. For determining the time of the onset of ring contraction, the ring diameter was measured as before, except the period before ring contraction was now also included. Diameters were converted to circumferences, and scatter plots of circumference versus time were made in Excel, from which the approximate time at which ring contraction begins was observed. To determine the initial ring circumference ($C0$), the average circumference at times before ring contraction onset was measured. A straight line ($y = m \times t + c$) was fitted to the contraction data at times later than the approximate onset of ring contraction. Then, y was set equal to $C0$ in the equation of the straight line, and the corresponding value of t was found, which was set as the time of the onset of ring contraction.

Generating normalized intensity kymographs of contracting rings

To generate the normalized intensity kymographs shown in Figure 4A and Supplemental Figure S1F, we first made face-on time-lapse movies of contracting rings as previously described. We did not perform any additional preprocessing, such as background subtraction, on these images. We then used semiautomated custom imageJ macros to generate the kymographs, which we describe below.

First, an oval ROI was drawn along the perimeter of the ring, and the plug-in "Polar Transformer" was used to convert the ring into a straight line that was orientated vertically. This process was repeated at each timestep, modifying the ROI as necessary as the ring contracted.

Next, we reduced the impact of the anisotropic point spread function that caused the fluorescence at the top and bottom of our rings to appear more spread out than at the sides, which makes the fluorescence at the top and bottom of the ring appear to be less intense than on the sides. To do this, we drew rectangular ROIs around the ring fluorescence in each of our linearized images, and then horizontally summed the intensity within these ROIs, generating an image with a single column of pixels, the values of which correspond to the summed fluorescence intensity at each angular position around the ring. These individual images were then concatenated together to produce a heatmap of the fluorescence intensity in the ring during contraction.

The density of many ring proteins changes as the ring contracts, usually becoming more concentrated. Because this could mask the behavior that we are interested in, we corrected for this by normal-izing the intensity in our intensity kymographs, so that the total fluorescence intensity in the ring remained constant over time. To do this, we measured the total intensity in the first column of the heatmap (i.e., the first timepoint), I_{first}. Then, we measured the total intensity in all of the subsequent columns, I_i in the ith column, and then multiplied all the pixel values in each column by the number I_{first}/I_i, so that the total intensity in each of the columns was now equal.

Actin segmentation

To produce normalized intensity kymographs for contracting rings in cells expressing LAGFP (Supplemental Figure S1F), we first needed to segment out the ring fluorescence, in order to avoid also including actin patches and cables that are next to the ring in our analysis. We did so using cells that coexpressed Cdc15-tdtomato, and using the fluorescence signal from the Cdc15 to threshold the ring, using a semiautomated custom ImageJ macro.

First, in the Cdc15-tdtomato channel, we measured the SD in the cellular background from a single z-slice. We then performed nonlocal means denoising, using the plug-in of the same name, and using our measured SD for the input value of "sigma" in the plug-in. Then we performed a background subtraction on the resulting image.

Next, we needed to perform thresholding. To do this, we separated the time-lapse image into individual stacks, corresponding to each timepoint in the image. We then applied thresholding to each individual stack (Image/Adjust/Threshold…), using the "IsoData" method of thresholding, and using the entire stack histogram to calculate the threshold. The individual stacks were then concatenated back together, and the resulting binary mask was used to extract the ring fluorescence from the LAGFP channel. From these segmented images, we then generated the normalized linearized intensity maps as previously described.

Segmentation of CW stained cells

To generate the segmented images in Figure 4C, images of CW stained cells were converted into a binary image using the "Threshold…" function (Image/Adjust/Threshold…) with the "Yen" automated threshold. This binary mask was multiplied with the original image to produce an image only containing the high-intensity pixels in the septum. Face-on views were then generated as described above. To view the cell wall signal in the images, an ROI was drawn around the cell in a region adjacent to the septum. This ROI was duplicated (Image/Duplicate…), resliced, and then the resultant image was sum intensity projected to produce a strong cell wall signal. Background subtraction was applied to this image, and then the septum and cell wall images were combined to produce the images shown in Figure 4C.

Fitting of GMM to histogram of peeling events

Fitting of GMMs to our data sets was performed using the "fitgmdist" function in MATLAB. A GMM is fitted directly to the data, rather than to the histogram, so the optimum GMM is independent of the appearance of the histogram. Custom MATLAB scripts were used to generate models with between one and five components (i.e., number of individual Gaussians), and select which of these produced the best fit, based on which model had the lowest AIC (Akaike Information Criterion) value. We also calculated the Akaike weights/probabilities for each model, using the formula

$$w_i\,(\text{AIC}) = exp\left\{-0.5 \cdot \left[\text{AIC}_i - \min(\text{AIC})\right]\right\} \Big/ \sum_{i=1}^{N} exp\left\{-0.5 \cdot \left[\text{AIC}_i - \min(\text{AIC})\right]\right\}$$

(Wagenmakers and Farrell, 2004), where w_i is the weight/probability for the ith model, AIC_i is the AIC value for the ith model, min(AIC) is the minimum AIC value from all the models, and N is the number of models (five). Using this, we obtained probabilities for models containing one to five components of 0.0045, 0.0365, 0.91, 0.0441, and 0.0048 for *adf1*-M2 cells, and 0.0001, 0.1284, 0.6469, 0.2099, and 0.0148 for *adf1*-M3 cells, indicating that a three-component model was the best fit for both sets of data.

REFERENCES

Cheffings TH, Burroughs NJ, Balasubramanian MK (2016). Actomyosin ring formation and tension generation in eukaryotic cytokinesis. Curr Biol 26, R719–R737.

Chen Q, Pollard TD (2011). Actin filament severing by cofilin is more important for assembly than constriction of the cytokinetic contractile ring. J Cell Biol 195, 485–498.

Chew TG, Huang J, Palani S, Sommese R, Kamnev A, Hatano T, Gu Y, Oliferenko S, Sivaramakrishnan S, Balasubramanian MK (2017). Actin turnover maintains actin filament homeostasis during cytokinetic ring contraction. J Cell Biol 216, 2657–2667.

Courtemanche N, Pollard TD, Chen Q (2016). Avoiding artefacts when counting polymerized actin in live cells with LifeAct fused to fluorescent proteins. Nat Cell Biol 18, 676–683.

Green AR, Paluch E, Oegema K (2012). Cytokinesis in animal cells. Annu Rev Cell Dev Biol 28, 29–58.

Jodoin JN, Coravos JS, Chanet S, Vasquez CG, Tworoger M, Kingston ER, Perkins LA, Perrimon N, Martin AC (2015). Stable force balance between epithelial cells arises from F-actin turnover. Dev Cell 35, 685–697.

Laplante C, Berro J, Karatekin E, Hernandez-Leyva A, Lee R, Pollard TD (2015). Three myosins contribute uniquely to the assembly and constriction of the fission yeast cytokinetic contractile ring. Curr Biol 25, 1–11.

Laplante C, Huang F, Tebbs IR, Bewersdorf J, Pollard TD (2016). Molecular organization of cytokinesis nodes and contractile rings by super-resolution fluorescence microscopy of live fission yeast. Proc Natl Acad Sci USA 113, E5876–E5885.

McDonald NA, Lind AL, Smith SE, Li R, Gould KL (2017). Nanoscale architecture of the *Schizosaccharomyces pombe* contractile ring. Elife 6, 1–23.

Moreno S, Klar A, Nurse P (1991). Molecular genetic analysis of fission yeast *Schizosaccharomyces pombe*. Methods Enzymol 194, 795–823.

Murthy K, Wadsworth P (2005). Myosin-II-dependent localization and dynamics of F-actin during cytokinesis. Curr Biol 15, 724–731.

Nakano K, Mabuchi I (2006). Actin-depolymerizing protein Adf1 is required for formation and maintenance of the contractile ring during cytokinesis in fission yeast. Mol Biol Cell 17, 1933–1945.

Nguyen L, Swulius MT, Aich S, Mishra M, Jensen GJ (2018). Coarse-grained simulations of actomyosin rings point to a nodeless model involving both unipolar and bipolar myosins. Mol Biol Cell 29, 1318–1331.

Oelz DB, Rubinstein BY, Mogilner A (2015). A combination of actin treadmilling and cross-linking drives contraction of random actomyosin arrays. Biophys J 109, 1818–1829.

Pelham R, Chang F (2002). Actin dynamics in the contractile ring during cytokinesis in fission yeast. Nature 419, 82–86.

Pollard TD (2010). Mechanics of cytokinesis in eukaryotes. Curr Opin Cell Biol 22, 50–56.

Pollard TD (2017). Nine unanswered questions about cytokinesis. J Cell Biol 216, 3007–3016.

Srivastava V, Robinson DN (2015). Mechanical stress and network structure drive protein dynamics during cytokinesis. Curr Biol 25, 663–670.

Stachowiak MR, Laplante C, Chin HF, Guirao B, Karatekin E, Pollard TD, O'Shaughnessy B (2014). Mechanism of cytokinetic contractile ring constriction in fission yeast. Dev Cell 29, 547–561.

Thiyagarajan S, Munteanu EL, Arasada R, Pollard TD, O'Shaughnessy B (2015). The fission yeast cytokinetic contractile ring regulates septum shape and closure. J Cell Sci 128, 3672–3681.

Thiyagarajan S, Wang S, O'Shaughnessy B (2017). A node organization in the actomyosin contractile ring generates tension and aids stability. Mol Biol Cell 28, 3286–3297.

Vavylonis D, Wu J-Q, Hao S, O'Shaughnessy B, Pollard TD (2008). Assembly mechanism of the contractile ring for cytokinesis by fission yeast. Science 319, 97–100.

Wagenmakers E-J, Farrell S (2004). AIC model selection using Akaike weights. Psychon Bull Rev 11, 192–196.

Wang N, Lo Presti L, Zhu YH, Kang M, Wu Z, Martin SG, Wu JQ (2014). The novel proteins Rng8 and Rng9 regulate the myosin-V Myo51 during fission yeast cytokinesis. J Cell Biol 205, 357–375.

Wollrab V, Thiagarajan R, Wald A, Kruse K, Riveline D (2016). Still and rotating myosin clusters determine cytokinetic ring constriction. Nat Commun 7, 1–9.

Wu J, Kuhn JR, Kovar DR, Pollard TD (2003). Spatial and temporal pathway for assembly and constriction of the contractile ring in fission yeast cytokinesis. Dev Cell 5, 723–734.

Wu J-Q, Pollard TD (2005). Counting cytokinesis proteins globally and locally in fission yeast. Science 310, 310–314.

Yumura S (2001). Myosin II dynamics and cortical flow during contractile ring formation in *Dictyostelium* cells. J Cell Biol 154, 137–145.

Zambon P, Palani S, Kamnev A, Balasubramanian MK (2017). Myo2p is the major motor involved in actomyosin ring contraction in fission yeast. Curr Biol 27, R99–R100.